Sustainable Chemical Engineering
http://ojs.wiserpub.com/index.php/SCE/

UNIVERSAL WISER PUBLISHER

Research Article

Simple, Green and Low-Cost Ni Nanoparticles/Tissue-Derived Nitrogen-Doped Porous Carbon Nanocomposites as an Efficient Electrocatalyst for Methanol Oxidation Reaction

Jiajie Lin[1], Jingchuang Zhao[1], Huiyan Fang[1], Changhui Tan[1,2], Yancai Li[1,2*]

[1]College of Chemistry, Chemical Engineering and Environment, Minnan Normal University, Zhangzhou, P. R. China
[2]Fujian Province Key Laboratory of Modern Analytical Science and Separation Technology, Minnan Normal University, Zhangzhou, P. R. China
E-mail: liyancai@mnnu.edu.cn

Received: 16 May 2023; **Revised:** 22 June 2023; **Accepted:** 1 July 2023

Abstract: In this work, green and low-cost Ni Nanoparticles/Tissue-derived Nitrogen-doped Porous Carbon Nanocomposites (NiNPs/T-dNPCNs) are prepared through a simple one-step pyrolysis process. The surface morphology and composition of the NiNPs/T-dNPCNs are characterized by X-Ray Diffraction (XRD), Inductively Coupled Plasma-Optical Emission Spectrometer (ICP-OES), Scanning Electron Microscopy (SEM), Transmission Electron Microscopy (TEM) and X-ray Photoelectron Spectra (XPS). The NiNPs/T-dNPCNs modified glassy carbon electrode (NiNPs/T-dNPCNs/GCE) exhibits good electrocatalytic activity to Methanol Oxidation Reaction (MOR) in alkaline solution. Among them, the mass activity of the NiNPs/T-dNPCNs$_{800}$ (carbonization at 800 ℃) is 3,349 mA · mg$_{Ni}^{-1}$, which is much higher than that of the NiNPs/T-dNPCNs carbonized at other temperatures (600, 700, 900 ℃). In addition, the mass activity of the NiNPs/T-dNPCNs$_{800}$ is 6.91 times higher than that of the commercial Pt/C. The NiNPs/T-dNPCNs$_{800}$/GCE also displays high stability, fast reaction kinetics and well resistance to carbon monoxide poisoning. Therefore, as a new biomass-derived non-noble metal MOR catalyst, the NiNPs/T-dNPCNs$_{800}$ will play an inspirational role in the development of MOR catalyst.

Keywords: nickel nanoparticles, tissue-derived nitrogen-doped porous carbon, electrocatalytic, methanol oxidation reaction, alkaline

1. Introduction

Direct Methanol Fuel Cell (DMFC) is a clean and sustainable energy conversion system. It exhibits the advantages of small size, high energy density and environmental friendliness. Hence, it has a profound application value in new energy vehicles and portable energy storage equipment.[1,2] Methanol Oxidation Reaction (MOR) is a key reaction of DMFC, and its rate depends on the anodic catalyst. At present, the best catalyst is a platinum-based catalysts for anodic MOR. However, the disadvantages of platinum-based catalyst, such as high price and easily poisoned by carbon oxide intermediates (CO),[3] have hindered the commercialization of DMFC.[4,5] Therefore, in order to eliminate the obstacles to the commercialization of DMFC, the development of non-noble metal catalysts with high efficiency and CO poisoning

DOI: https://doi.org/10.37256/sce.4220233054

resistance have become an important topic.

Among non-noble metal catalysts, nickel-based catalysts are considered to be one of the most valuable MOR catalysts, based on their high catalytic activity and low cost.[6,7] Positive nickel ions (Ni^{2+} and Ni^{3+}) will provide a stable ladder for electron transfer during the MOR. Unpaired d-electrons or empty d-orbitals form bonds with the oxidized form of Ni (NiOOH, Ni^{3+}), which are available for bond formation with adsorbed species or redox intermediates.[6,8] Recent research on MOR catalytic reaction shows that carbon-supported Ni-based materials are emerging nanomaterials for energy storage applications. Sun et al.[9] through an *in-situ* laser irradiation approach was developed to fabricate S, N dual-doped multi-walled carbon nanotubes coupled with NiO nanoparticles (NiO/S, N-CNTs) as non-platinum catalysts for MOR assisted. NiO/S, N-CNTs showed a high primary methanol oxidation activity of 2,200 $mA \cdot mg^{-1}$, long-term durability with 65.8% of mass activity maintained after 40,000 s, and an excellent methanol saturation concentration of 13 M. Wu et al.[10] used pyrolysis to generate Ni/N-C@$_{500}$ composites (act as active electrocatalysts for MOR), while nitrogen-doped carbon substrates acted as conductive carriers to promote electron transfer and protect active Ni nanocrystals. The Ni/N-C@$_{500}$ electrode attained a current density of 101 $mA \cdot cm^{-2}$ at 1.55 V (Saturated Calomel Electrode) of under 1 M KOH with 1 M CH_3OH, at 50 $mV \cdot s^{-1}$. In addition, Zhu et al.[11] synthesized three-dimensional graphene (3D-G) by Hummer's method, followed by the template-assembly method and then deposited Ni particles by chemical reduction method. The as-synthesized Ni/3D-G illustrated an onset potential of ~0.45 V (vs. Hg/HgO) and an overpotential of ~0.69 V (Hg/HgO) at 64.7 $mA \cdot cm^{-2}$. But these methods are complicated, multistep and used hazardous chemicals (Hummer's method). However, the catalytic activity and stability of nickel-based materials need to be further improved before they can be commercialized.

In the process of electrocatalytic reaction, the Nickel Nanoparticles (NiNPs) with small sizes will aggregate into larger ones, resulting in a decrease in durability. It is worth noting that the MOR durability can be improved by immobilization of the NiNPs with a suitable carrier.[12] Until now, a variety of carriers have been used in MOR catalysts, such as mesoporous carbon,[13] carbon nanofibers,[14] graphene oxide,[15,16] and MoO_2[17] etc. Because carbon-based materials have a unique structure and electrochemical properties, such as large active surface area, strong interaction with metal particles; excellent electrical conductivity, they can promote electron transfer in electrocatalytic processes; well chemical stability, reduce the aggregation or corrosion of nanoparticles under harsh electrochemical conditions, maintain the structural integrity of the composite material to improve the durability of the catalyst.[9,12,16,18] Recently, carbon nanomaterials prepared from biomass (such as natural apples,[19] bean dregs,[20] bagasse[21]) have attracted wide attention due to their nontoxicity, low cost and excellent chemical stability. Typically, Liu et al.[22] developed a new three-dimensional layered porous carbon structure using a simple template-free synthesis route from tissues. The porous structure can not only enrich the active sites, but also transport the reaction-relevant species (including the reactants and gas bubbles), which can improve the kinetics of catalytic reactions.[23-26] Guo et al.[12] constructed Ni/NiO heterojunction (Ni/NiO@NC-T) supported on N-doped carbon substrate by pyrolysis, using sodium alginate as carbon source. The optimum Ni/NiO@NC$_{600}$ sample had excellent activity for MOR with the current density (j) of 225 $mA \cdot cm^{-2}$ at 1.6 V under an alkaline medium. In addition, biomass generally contains a certain amount of nitrogen. Recent works have proved that the doping of N can adjust the electronic structure and conductivity of the material, N doping also increases the electronic cloud at the junction point which also facilitates the catalytic application, after doping the defect can increase active spots for deposition active materials and it may improve the dispersion and avoid agglomeration.[27-29] Therefore, nitrogen-doped biomass-derived carbon is expected to be an excellent catalyst carrier.

In this work, by a simple one-step pyrolysis process, we have developed a green and low-cost Ni Nanoparticles/Tissue-derived Nitrogen-doped Porous Carbon Nanocomposites (NiNPs/T-dNPCNs), with a large number of nickel nanoparticles embedded in the carbon layer. The NiNPs/T-dNPCNs were characterized by X-Ray Diffraction (XRD), Inductively Coupled Plasma-Optical Emission Spectrometer (ICP-OES), Scanning Electron Microscopy (SEM), Transmission Electron Microscopy (TEM) and X-ray Photoelectron Spectra (XPS). The NiNPs/T-dNPCNs modified glassy carbon electrode (NiNPs/T-dNPCNs/GCE) displays good electrocatalytic activity to MOR in alkaline, and the effect of carbonization temperature of the NiNPs/T-dNPCNs on the electrocatalytic performance was also studied. The results show that the optimal carbonization temperature is 800 ℃. The NiNPs/T-dNPCNs$_{800}$ has the highest electrocatalytic activity, the fastest reaction kinetics, excellent stability and resistance to carbon monoxide poisoning.

2. Experimental section

2.1 *Chemicals*

The tissues (consisting of abundant plant cellulose fibers) were afforded by 'Mind Act Upon Mind' and obtained from a supermarket in Zhangzhou. Methanol (CH_3OH AR, 99.5%), ethanol (C_2H_5OH AR, 99.5%), potassium hydroxide (KOH AR, 85%) and potassium chloride (KCl AR, 99.5%) were obtained from Xilong Chemical Co., Ltd. (Shantou, China). Nickel (II) acetate tetrahydrate ($Ni(AC)_2 \cdot 4H_2O$ AR, 99%) and platinum on carbon (10% Pt/C, Identification of product: P111329) were obtained from Aladdin Reagent Co., Ltd. (Shanghai, China). Nafion was acquired from Sigma-Aldrich. All of the chemical reagents are analytical grade and used without further purification. Ultrapure water was obtained from the Milli-Q system Millipore (USA).

2.2 *Instruments and measurements*

XRD patterns were obtained on Pan-altical X'Pert-pro MPD using Cu Kα radiation. SEM images were taken on Zeiss supra55 at 5 kV. TEM images were observed by JEM 2,100 F at 200 kV. The high-Angle Annular Dark Field-Scanning Transmission Electron Microscopy (HAADF-STEM) and the elemental mapping images were obtained from FEI Tecnai G2 F30 at 300 kV. The actual loading of Ni in the prepared catalyst had been determined by Inductively Coupled Plasma-Optical Emission Spectroscopy (ICP-OES, Agilent 720ES). The XPS was measured by Escalab 250xi at 15 kV, with C 1s of 284.6 eV binding energy standards for charge correction.

Electrochemical experiments were investigated by a CHI 650D electrochemical workstation (CH Instruments, Inc. Shanghai) at room temperature. All electrochemical experiments have been measured in a typical three-electrode system with a bare Glassy Carbon Electrode (GCE, Φ = 3 mm, 0.071 cm^2). The modified or unmodified glassy carbon electrode was used as the working electrode, and the Pt wire and Ag/AgCl (3.0 M KCl) electrode were used as the counter and reference electrodes, respectively.

The MOR results were obtained by Cyclic Voltammetry (CV) in 1 M CH_3OH and 1 M KOH, at 50 $mV \cdot s^{-1}$ and potential range 0.2-0.8 V (vs. RHE, Reversible Hydrogen Electrode) (converted by Nernst equation $E_{RHE} = E_{Ag/AgCl} + 0.059 * pH + E^{\theta}_{Ag/AgCl}$).[4]

2.3 *Synthesis of the NiNPs/T-dNPCNs*

In a small beaker, 10 mL $Ni(AC)_2 \cdot 4H_2O$ (0.06 mol L^{-1}) solution was prepared as a dipping solution. 2.0 g tissues were cut into small pieces and then were put into the beaker to absorb the dipping solution. The soaked tissues were transferred to a porcelain ark. The porcelain ark was placed in a tube furnace, heated to 800 °C at the heating rate of 5 °C $\cdot$ min^{-1} under a flowing N_2 atmosphere for 3 h, and naturally cooled to room temperature to obtain black products. In the mortar, the black product was ground to a powder and was named NiNPs/T-dNPCNs$_{800}$. The as-prepared products were directly used without any post-treatment.

The materials carbonized at 600 °C, 700 °C and 900 °C were named as the NiNPs/T-dNPCNs$_{600}$, the NiNPs/T-dNPCNs$_{700}$ and the NiNPs/T-dNPCNs$_{900}$, respectively.

2.4 *Preparation of the modified electrode*

Firstly, the catalyst ink was prepared. 1.0 mg of the NiNPs/T-dNPCNs or 10% Pt/C, 990 μL ultrapure water and 10 μL 5 wt % Nafion solution were put into a centrifuge tube, the mixture was ultrasound for 30 min. Secondly, the GCE was polished to a mirror surface using 1.0 μm, 0.3 μm and 0.05 μm aluminum oxide powder on nylon cloth and suede, respectively. Finally, 4 μL catalyst ink was carefully dropped onto the GCE surface immediately using a micropipette and dried naturally at room temperature. The modified electrodes were named the NiNPs/T-dNPCNs$_x$/GCE (x = 600, 700, 800, 900 °C, respectively) or Pt/C/GCE.

3. Results and discussion

3.1 *Composition and structural characterization*

The morphology of the NiNPs/T-dNPCNs carbonized at different temperatures was investigated by SEM and TEM. As shown in SEM images of Figure S1A-D (see Appendix), the different NiNPs/T-dNPCNs display overall fiber morphology, which is derived from the plant fibers in the wood tissues. The detailed fiber surface of the different NiNPs/T-dNPCNs was magnified by SEM and TEM images in Figure 1. The surface of the NiNPs/T-dNPCNs$_{600}$ (SEM of Figure 1A) is smooth and evenly distributed with fine NiNPs, but there has no pore structure from TEM image in Figure 1E. The NiNPs/T-dNPCNs$_{700}$ also displays a smooth surface and distributed NiNPs; however, the size of NiNPs increased significantly, and there appear small pores on its surface and interior, as shown in Figure 1B and Figure 1F. As to the NiNPs/T-dNPCNs$_{800}$, the pores become larger and more pronounced when the carbonization temperature rises to 800 ℃ (Figure 1C and Figure 1G). At the same time, the NiNPs were also significantly larger, and some of them were hiding in the pores. However, as the carbonization temperature increased to 900 ℃, the number of pores on the surface decreased considerably (Figure 1D and Figure 1H), and the surface of the catalyst became smoother than that of the NiNPs/T-dNPCNs$_{800}$ (Figure 1D), possibly due to the high temperature which leads to the sintering of carbon on the material surface. This sintering may result in the active center of NiNPs being embedded deeply in the carbon material and unable to play a catalytic role. To sum up, with the increasing carbonization temperature, the size of NiNPs and the abundance of pores tend to increase. Among them, the nickel active center of the NiNPs/T-dNPCNs$_{800}$ is fully exposed because of its rich pore structure, which may help to improve its electrocatalytic activity. In addition, the Ni mass percentage of the NiNPs/T-dNPCNs$_x$ (x = 600, 700, 800 and 900 ℃) was analyzed by the ICP-OES technique, and the results are 5.99 wt. %, 6.85 wt. %, 7.48 wt. % and 6.58 wt. %, respectively.

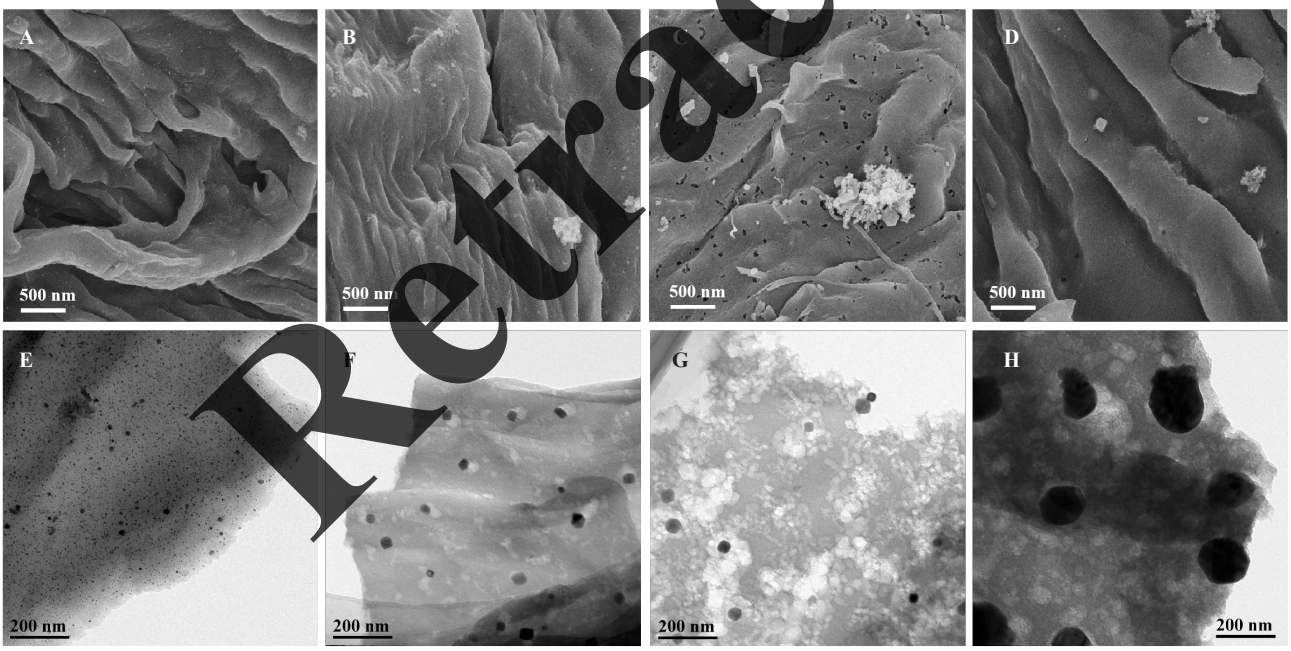

Figure 1. SEM and TEM images of the NiNPs/T-dNPCNs$_{600}$ (A) and (E), the NiNPs/T-dNPCNs$_{700}$ (B) and (F), the NiNPs/T-dNPCNs$_{800}$ (C) and (G), the NiNPs/T-dNPCNs$_{900}$ (D) and (H)

The surface morphology and composition of the NiNPs/T-dNPCNs were further observed using TEM and elemental mapping, as shown in Figure 2 and Figure S2 (see Appendix). The rich surface openings and pore structure of the NiNPs/T-dNPCNs$_{800}$ can be clearly observed from the TEM images in Figure 2A. Notably, the porosity of the NiNPs/T-dNPCNs$_{800}$ will be helpful for transferring the reaction-relevant species (including the reactants and gas

bubbles) and in turn improve the reaction kinetics.[22-26] As exhibited in High-Resolution TEM (HRTEM) image of Figure 2B, the lattice fringes of about 0.201 nm belongs to the crystal faces of Ni (111) with fcc-structure (JCPDS No.01-087-0712).[30] The lattice spacing of the NiNPs/T-dNPCNs$_{600}$, the NiNPs/T-dNPCNs$_{700}$ and the NiNPs/T-dNPCNs$_{900}$ was 0.200 nm, 0.200 nm and 0.202 nm, respectively, which analyzed by HRTEM in Figure S2 (see Appendix). Figure 2C-G displays the HAADF-STEM and the elemental mapping images of the NiNPs/T-dNPCNs$_{800}$, in which reveals the homogeneous distribution of the four elements of C, Ni, N and O in the NiNPs/T-dNPCNs$_{800}$.

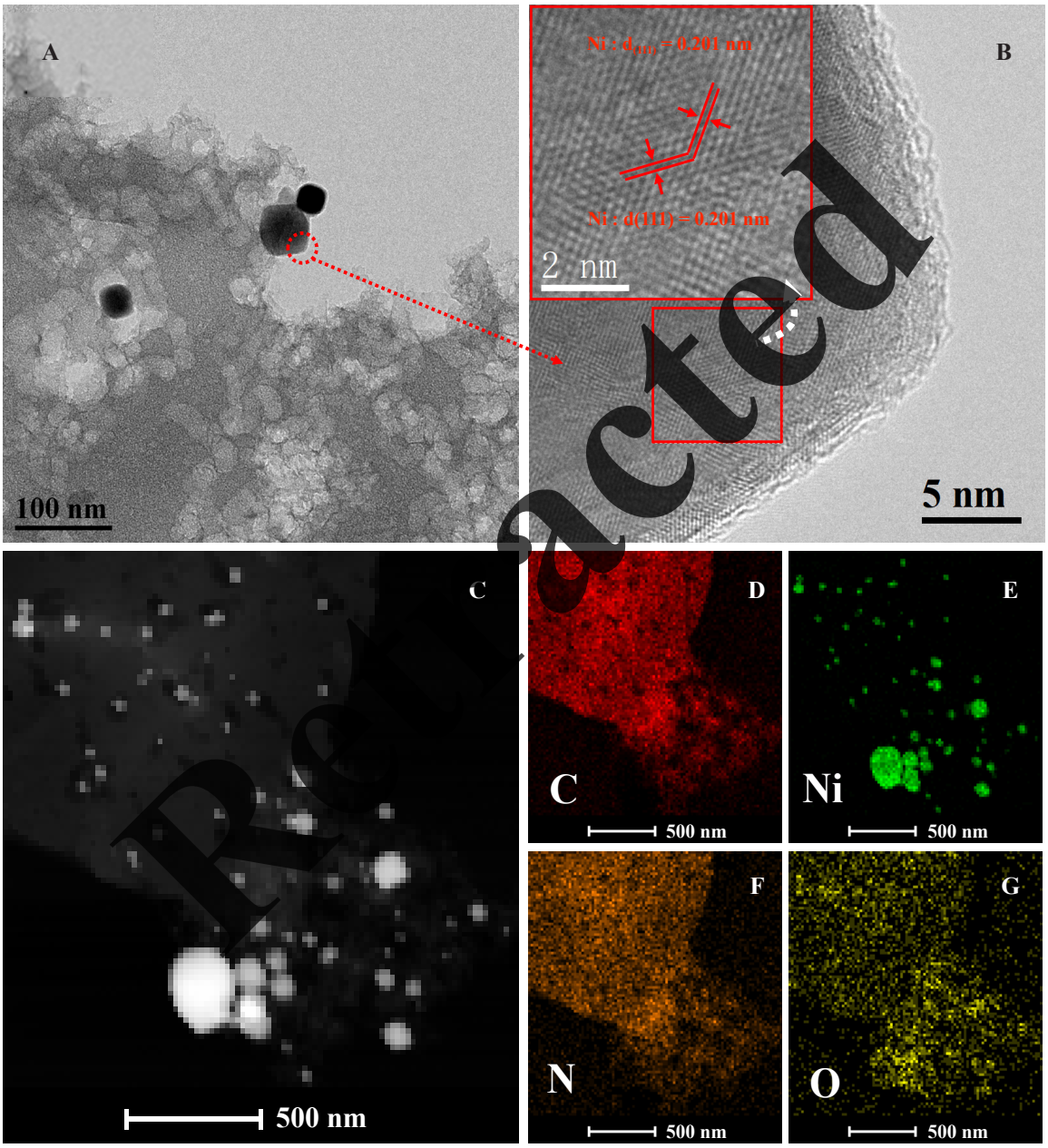

Figure 2. (A) TEM image of the NiNPs/T-dNPCNs$_{800}$, (B) HRTEM image of the partially area marked in (A), (C) HAADF-STEM and the corresponding elemental mapping images of (D) C, (E) Ni, (F) N and (G) O

The structure and composition of the NiNPs/T-dNPCNs carbonization at different temperatures were investigated by XRD, as shown in Figure 3. The diffraction peaks at 44.52°, 51.96° and 76.46° can be indexed to (111), (200) and (220) planes of pure Ni with fcc-structure (JCPDS No. 01-087-0712).[30] It is worth mentioning that the lattice spacing results are consistent well with the TEM analysis. In addition, the broad peak from 15.00° to 31.00° can be attributed to graphene-like carbon (d(002), JCPDS No. 41-1487).[11,31] At a carbonization temperature of 900 ℃, there has an obviously small peak at 26.10°, which could be attributed to the crystallization of the C(002) plane at high temperature.

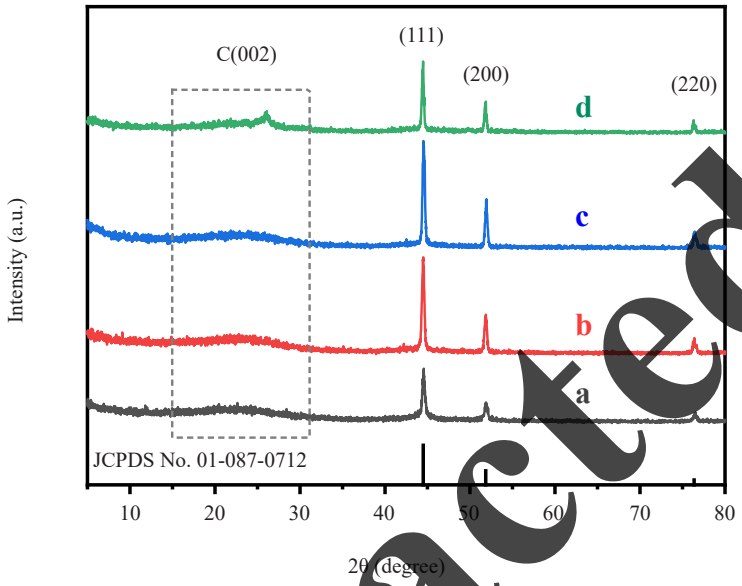

Figure 3. XRD patterns of the NiNPs/T-dNPCNs$_{600}$ (a), the NiNPs/T-dNPCNs$_{700}$ (b), the NiNPs/T-dNPCNs$_{800}$ (c) and the NiNPs/T-dNPCNs$_{900}$ (d)

The surface chemical composition of the prepared materials was characterized by XPS. As shown in the XPS survey spectra of the NiNPs/T-dNPCNs in Figure 4A, it can be clearly observed C and O signals, and also the weak N and Ni characteristic peaks. Meanwhile, the contents of C, N, O and Ni elements were listed in Figure 4B. XPS spectra of C 1s, N 1s, O 1s and Ni 2p of the NiNPs/T-dNPCNs were fitted by peaks (Figure S3 (see Appendix)). The high-resolution C 1s XPS spectrum of the NiNPs/T-dNPCNs$_{800}$ was assigned three small peaks (Figure S3I (see Appendix)), which can be classified as C = C sp^2 (284.75 eV), C-C sp^3/C = N sp^2 (285.75 eV) and C = O/C-N (289.65 eV). The weak N 1s XPS spectrum of the NiNPs/T-dNPCNs$_{800}$ indicates that there is a little nitrogen element on the surface layer of the NiNPs/T-dNPCNs$_{800}$ (Figure S3J (see Appendix)). The high-resolution O 1s XPS spectrum of the NiNPs/T-dNPCNs$_{800}$ can be deconvoluted to three peaks, corresponding to O-C = O/C = O (531.55 eV) and C-O (532.65 eV) and the physically adsorbed water molecules (533.9 eV) (Figure S3K (see Appendix)).[10,18,32] As shown in Figure S3L (see Appendix), the Ni 2p spectrum of the NiNPs/T-dNPCNs$_{800}$ shows two spin-orbit splitting peaks at 856.45 eV (Ni 2p 3/2) and 874.1 eV (Ni 2p 1/2) followed with two vibrating satellite peaks at 861.95 eV and 880.9 eV. Furthermore, two fitting peaks located at the binding energy of 853.3 eV and 870.4 eV, should be attributed to Ni(0).[18,33] These peaks confirmed the presence of metallic Ni and its oxidize surface. XPS data confirmed the presence of oxygen-containing groups with low concentrations. This should be attributed to nickel hydroxide or oxide which is produced quickly on the nickel surface exposed to air or aqueous solution, but the negligible concentrations of these oxides on the sample surface are hard to detect by XRD.[1,34]

A

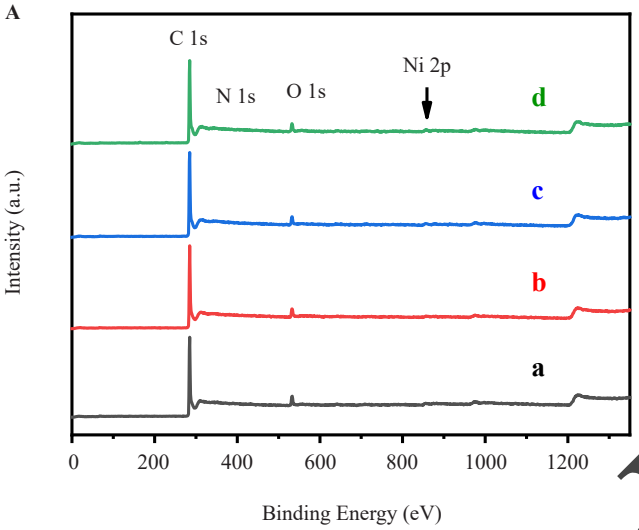

B

Sample	XPS elemental content (%)			
	C	N	O	Ni
Ni/T-dNPCNs6$_{00}$	92.76	0.7	5.93	0.61
Ni/T-dNPCNs$_{700}$	94.51	0.05	4.98	0.47
Ni/T-dNPCNs$_{800}$	94.05	1	4.37	0.58
Ni/T-dNPCNs$_{900}$	93.97	0.44	4.86	0.73

Figure 4. (A) XPS survey spectra of (a) the NiNPs/T-dNPCNs$_{600}$, (b) the NiNPs/T-dNPCNs$_{700}$, (c) the NiNPs/T-dNPCNs$_{800}$ and (d) the NiNPs/T-dNPCNs$_{900}$; (B) The content of each element on the surface of the NiNPs/T-dNPCNs

3.2 *Electrochemical and electrocatalytic performance*

The electrocatalytic oxidation process of methanol on nickel-based catalyst in alkaline medium is shown as follows:[10,30]

$$Ni + 2OH^- \rightarrow Ni(OH)_2 + 2e^- \quad (1)$$

$$Ni(OH)_2 + OH^- \rightarrow NiOOH + H_2O + e^- \quad (2)$$

$$NiOOH + CH_3OH \rightarrow Ni(OH)_2 + \text{products} \quad (3)$$

It can be seen from equation (2) that the formation of NiOOH is crucial in the process of methanol oxidation. These unpaired d-electrons and empty d-orbitals in NiOOH could form chemical bonds with the adsorbed small molecules, thus leading to catalytic oxidation reactions.[6] Therefore, in order to fully enrich the NiOOH, the NiNPs/T-dNPCNs were pretreated by Cyclic Voltammetry (CV) at 200 mV · s^{-1} for 50 cycles and 50 mV · s^{-1} for 20 cycles in 1 M KOH before the electrochemical performance test.[35]

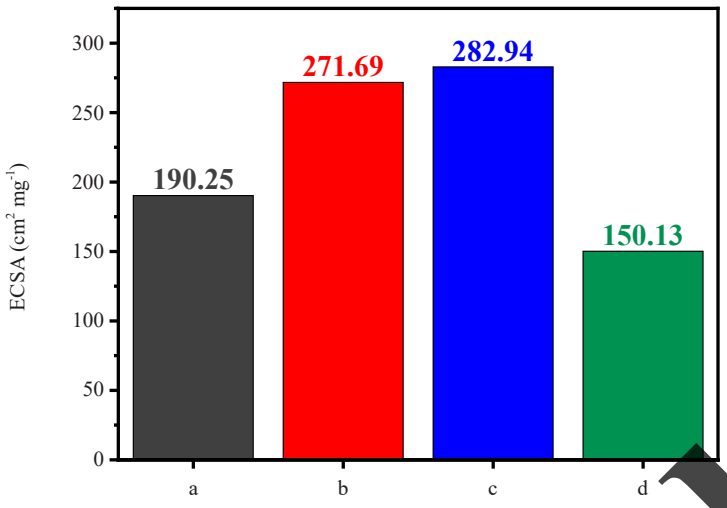

Figure 5. The ECSA of (a) the NiNPs/T-dNPCNs$_{600}$/GCE, (b) the NiNPs/T-dNPCNs$_{700}$/GCE, (c) the NiNPs/T-dNPCNs$_{800}$/GCE and (d) the NiNPs/T-dNPCNs$_{900}$/GCE in 1.0 M KOH

The Electrochemical Activity-specific Surface Area (ECSA) is one of the important indexes to evaluate the catalytic performance of a catalyst. In general, the ECSA of Ni-based materials is calculated by double capacitance (C_{dl}). The C_{dl} was calculated by the relation between the CV curves and the scan rates, in the non-Faradaic potential region. As shown in Figure S4A-D (see Appendix), CV curves were taken in the potential range from -0.10 V to -0.00 V (vs. Ag/AgCl) at various scan rates of 5, 10, 15, 20 and 25 mV·s^{-1} in 1.0 M KOH solution.[36-38] Figure S4A′-D′ (see Appendix) are the capacitive current ((I_a - I_c)/2) at -0.05 V vs. Ag/AgCl as a function of various scan rates, in which the C_{dl} is equal to the slopes. The C_{dl} of the NiNPs/T-dNPCNs$_{600}$/GCE (a), NiNPs/T-dNPCNs$_{700}$/GCE (b), NiNPs/T-dNPCNs$_{800}$/GCE (c) and NiNPs/T-dNPCNs$_{900}$/GCE (d) are 30.44 × 10^{-3}, 43.47 × 10^{-3}, 45.27 × 10^{-3}, 9.27 × 10^{-3} and 24.02 × 10^{-3} mF, respectively. According to the following formula:[36-38]

$$ECSA = C_{dl} / (C_s \times l) \quad (4)$$

C_s is the specific capacitance of the sample (C_s = 0.04 mF·cm^{-2} in KOH solution), and 'l' is the catalyst loading in 'mg' of the working electrode.[1] The ECSA of the NiNPs/T-dNPCNs$_{600}$/GCE (a), the NiNPs/T-dNPCNs$_{700}$/GCE (b), the NiNPs/T-dNPCNs$_{800}$/GCE (c) and the NiNPs/T-dNPCNs$_{900}$/GCE (d) were calculated as 190.25, 271.69, 282.94 and 150.13 cm^2·mg^{-1}, respectively, as shown in the histogram of Figure 5. The results illustrate that the NiNPs/T-dNPCNs$_{800}$ possesses the highest ECSA, which may be attributed to its abundant pore structure. In addition, the ECSA of the NiNPs/T-dNPCNs$_{900}$ was reduced significantly, which may be due to the excessive carbonization temperature resulting in carbon sintering. In addition, it is well known that carbon is an active species, the presence of only carbon materials would also hinder MOR, this also confirmed that only Ni NPs are the active site of MOR.[11,31,39-41]

The electrocatalytic properties of the NiNPs/T-dNPCNs/GCE were tested by CV at 50 mV·s^{-1} in 1 M KOH without and with 1.0 M CH_3OH (Figure 6). After the addition of 1.0 M CH_3OH, the NiNPs/T-dNPCNs/GCE all exhibit obvious oxidation and reduction peaks, and the NiNPs/T-dNPCNs$_{800}$/GCE shows the highest oxidation peak. Meanwhile, due to the oxidation of adsorption intermediates formed in the forward scan, an obvious anode peak appeared in the reverse scan, indicating that the NiNPs/T-dNPCNs had good anti-CO poisoning performance.[42,43] The lower onset potential means an easier oxidation process on the catalysts surface.[44,45] The onset potential of the NiNPs/T-dNPCNs$_{800}$/GCE was 0.353 V, which is lower than the MOR onset potential of the NiNPs/T-dNPCNs$_{600}$/GCE (0.369 V), the NiNPs/T-dNPCNs$_{700}$/GCE (0.366V) and the NiNPs/T-dNPCNs$_{900}$/GCE (0.359 V) (inset in the Figure 7A), suggested easier oxidation of methanol on the NiNPs/T-dNPCNs$_{800}$/GCE. The CV of the NiNPs/T-dNPCNs are all normalized by the mass percentage of Ni, as shown in Figure 7B. Mass Activity (MA, normalized by the Ni mass percentage of catalyst) and Specific Activity (SA, normalized by ECSA of catalyst) of the NiNPs/T-dNPCNs are calculated and

shown in the histogram of Figure 7C, which we can observe the NiNPs/T-dNPCNs$_{800}$/GCE displays the highest MA (3,349 mA·mg$_{Ni}^{-1}$) and SA (0.885 mA·cm^{-2}). The well-catalytic performance of the NiNPs/T-dNPCNs$_{800}$/GCE may have resulted in its abundant pore structure, the lowest onset potential and the highest ECSA. The superior catalytic activity of the NiNPs/T-dNPCNs$_{800}$ is compared with the published excellent catalysts in Table S1 (see Appendix). By comparison, the MA of the NiNPs/T-dNPCNs$_{800}$ exceeds that of most published Ni-based catalysts.

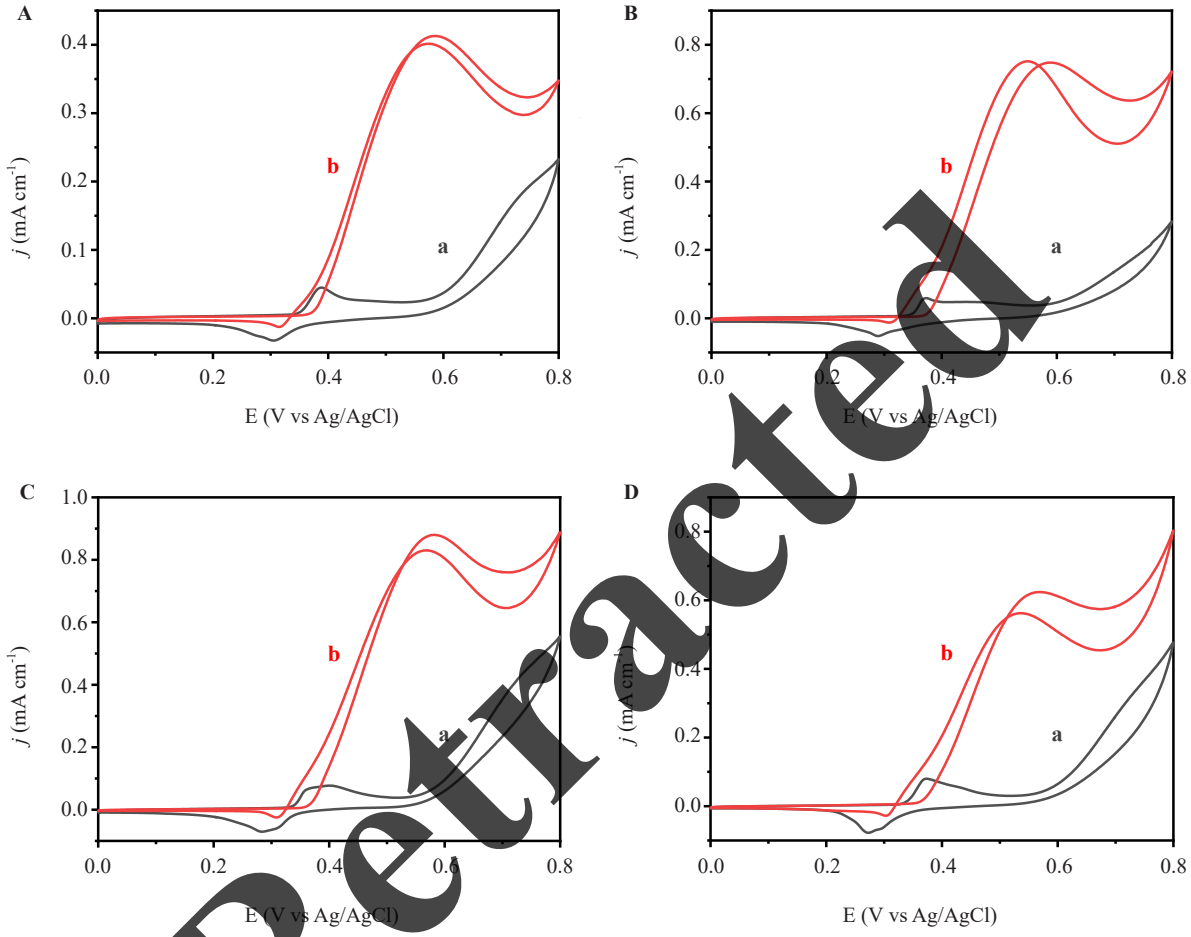

Figure 6. CV curves of the NiNPs/T-dNPCNs$_{600}$/GCE (A), the NiNPs/T-dNPCNs$_{700}$/GCE (B), the NiNPs/T-dNPCNs$_{800}$/GCE (C) and the NiNPs/T-dNPCNs$_{900}$/GCE (D) in 1.0 M KOH without (a) and with (b) 1.0 M CH_3OH, at 50 mV·s^{-1}

In order to explore the feasibility of MOR instead of OER to reduce energy consumption, the Linear Sweep Voltammetry (LSV) curves of the NiNPs/T-dNPCNs$_{800}$/GCE were performed in 1.0 M KOH solution without and with 1.0 M CH_3OH, as shown in Figure S5 (see Appendix). The NiNPs/T-dNPCNs$_{800}$/GCE has an obvious MOR peak (curve an of Figure S5 (see Appendix)). In addition, when the current density reaches 10 mA·cm^{-2}, MOR possesses an overpotential of 408 mV compared with OER (curve b of Figure S5 (see Appendix)), which indicates that MOR can be used as a Sacrificial Agent Oxidation Reaction (SAOR) to replace OER for efficient hydrogen production with low energy consumption.

Tafel slope is an important parameter, which is related to the kinetics of the MOR. The lower Tafel slope demonstrates the faster charge transfer across the electrocatalytic interface.[46] Moreover, a lower magnitude of the Tafel slope also shows that the active electrocatalyst has a higher tolerance to the poisoning species.[47] As shown in Figure 8A, the Tafel slopes of the NiNPs/T-dNPCNs$_{600}$/GCE (a), NiNPs/T-dNPCNs$_{700}$/GCE (b), NiNPs/T-dNPCNs$_{800}$/GCE (c) and NiNPs/T-dNPCNs$_{900}$/GCE (d) are 70.62, 49.21, 36.32 and 67.24 mV dec^{-1}, respectively. The NiNPs/T-dNPCNs$_{800}$/GCE

had the lowest Tafel slope compared with other catalysts. This demonstrates that the NiNPs/T-dNPCNs$_{800}$/GCE has good catalytic activity and anti-poisoning performance to the various toxic intermediate species, which is the main reason for its higher methanol electro-oxidation ability.[9] The stability of the catalysts was tested using chronoamperometry (CA) in a solution of 1.0 M KOH containing 1.0 M methanol. Figure 8B shows the CA curves of the NiNPs/T-dNPCNs at 0.60 V for 10,000 s. It can be seen obviously that the NiNPs/T-dNPCNs$_{800}$ maintains the maximum current density, which indicates that the NiNPs/T-dNPCNs$_{800}$ has outstanding resistance to carbon monoxide poisoning. Finally, the catalytic activity and stability of the NiNPs/T-dNPCNs$_{800}$ were also compared with the commercial Pt/C. The catalytic activity of the NiNPs/T-dNPCNs$_{800}$ is 6.91 times higher than that of the commercial Pt/C. (Figure 8C). Electrochemical stability of the NiNPs/T-dNPCNs$_{800}$ is much higher than that of the commercial Pt/C (Figure 8D).

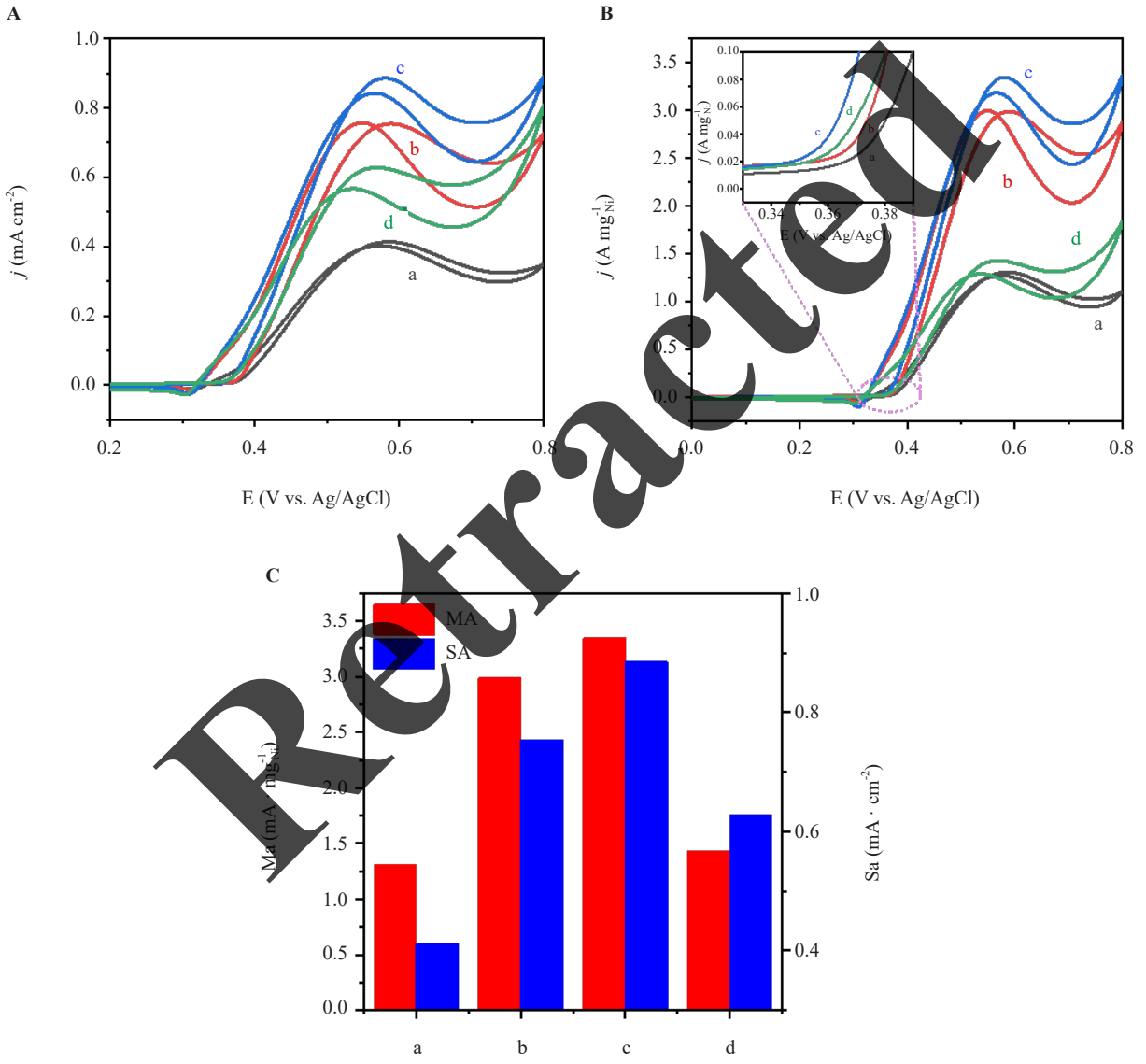

Figure 7. SA (A) and MA (B) of (a) the NiNPs/T-dNPCNs$_{600}$/GCE, (b) the NiNPs/T-dNPCNs$_{700}$/GCE, (c) the NiNPs/T-dNPCNs$_{800}$/GCE and (d) the NiNPs/T-dNPCNs$_{900}$/GCE in 1.0 M KOH containing 1.0 M CH_3OH, the scan rate of 50 mV · s^{-1}, the inset in Figure A is the enlarged onset potential part of the modified electrodes; (C) A histogram of MA and SA of the above four modified electrodes

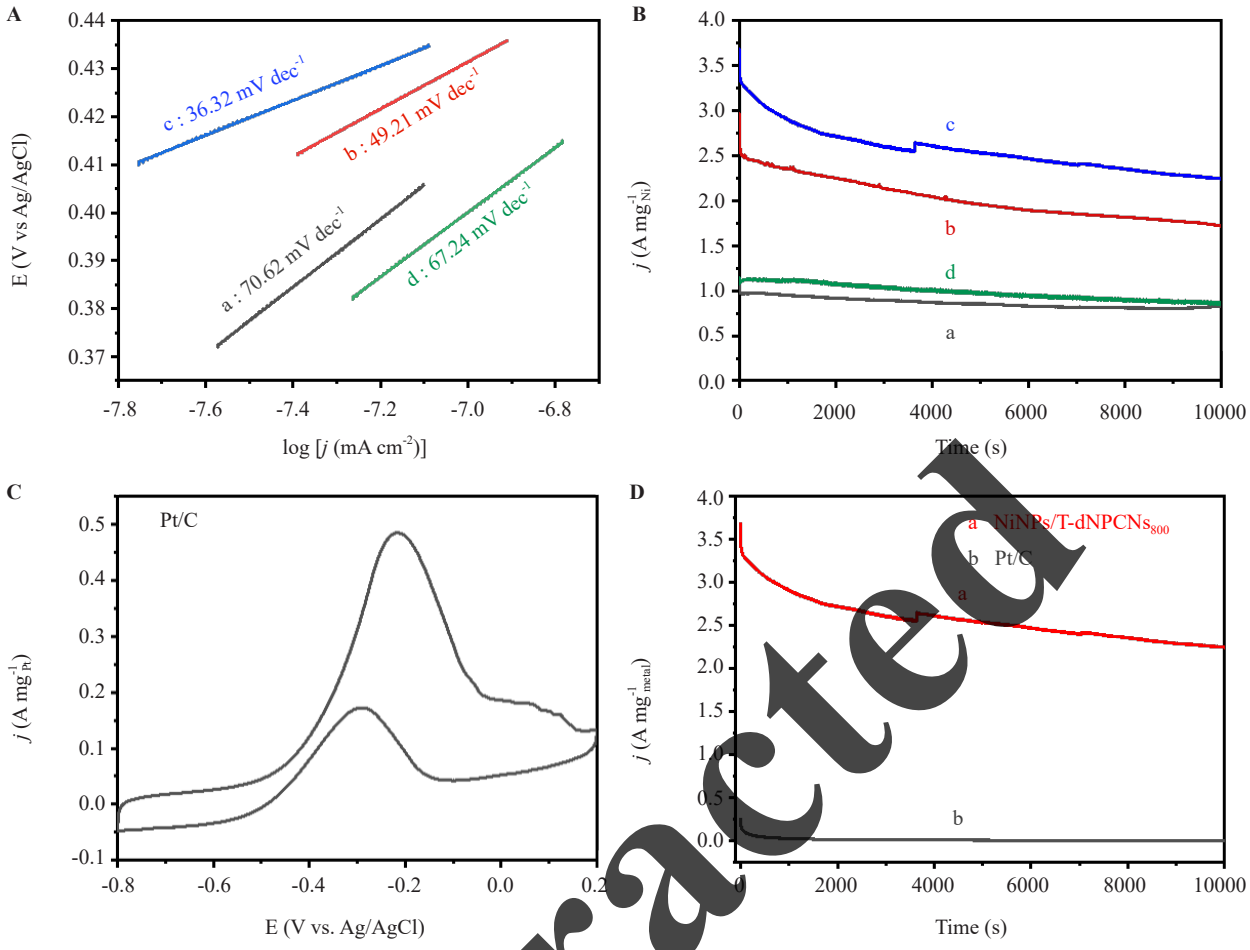

Figure 8. (A) Tafel plots and (B) I-t curves (for 10,000 s at 0.6 V vs. Ag/AgCl) of (a) the NiNPs/T-dNPCNs$_{600}$/GCE, (b) the NiNPs/T-dNPCNs$_{700}$/GCE, (c) the NiNPs/T-dNPCNs$_{800}$/GCE and (d) the NiNPs/T-dNPCNs$_{900}$/GCE; (C) CV of the Pt/C/GCE, scan rate: 50 mV·s^{-1}; (D) I-t curves for 10,000 s of the NiNPs/T-dNPCNs$_{800}$/GCE at 0.6 V, (a) and the Pt/C/GCE at 0.2 V, (b). All the above experiments were performed at 1.0 M KOH containing 1.0 M CH_3OH

4. Conclusion

In conclusion, the NiNPs/T-dNPCNs were prepared from tissues and $Ni(AC)_2 \cdot 4H_2O$ by one-step pyrolysis, as the cost-effective and noble metal-free MOR catalytic electrode. SEM, TEM, XRD, XPS and ICP-OES measurements reveal that the NiNPs/T-dNPCNs materials have been successfully prepared. It can be seen that the carbon matrices especially those containing rich pore structure significantly inhibit the aggregation of NiNPs nanocrystals in the preparation procedure. More importantly, the NiNPs/T-dNPCNs$_{800}$ inherently exhibited better MOR catalytic and superior stability in a long-term electrochemical process compared with the other three samples, in which the NiNPs/T-dNPCNs$_{800}$ exhibit the best electrocatalytic performance with high mass activity up to 3,349 mA·mg$_{Ni}^{-1}$. The NiNPs/T-dNPCNs$_{800}$/GCE also displays the fastest reaction kinetics and outstanding resistance to carbon monoxide poisoning. These results all illustrate that the use of a carbon matrix with a large surface area, abundant pore nanostructures, and excellent electron transport rate can effectively enhance the catalytic performances of the as-prepared and MOR electrocatalysts. Therefore, this green and low-cost NiNPs/T-dNPCNs$_{800}$ has great potential applications as MOR catalyst and should be of great significance in the reuse of biomass waste. At the same time, this work has heuristic significance for the research and development of biomass-derived carbon materials as MOR catalyst carriers.

Acknowledgments

The work was supported by the National Natural Science Foundation of China (21905125) and the Natural Science Foundation of Fujian province in China (No. 2020J01802).

Conflict of interest

The authors declare that they have no conflict of interest.

References

[1] Zhang, Y. Z.; Song, Y. Y.; Zhao, J. C.; Li, S. X.; Li, Y. C. Ultrahigh electrocatalytic activity and durability of bimetallic Au@Ni core-shell nanoparticles supported on rGO for methanol oxidation reaction in alkaline electrolyte. *J. Alloys. Compd*. **2020,** *822*, 153322.

[2] Ji, M. D.; Wang, J. L. Review and comparison of various hydrogen production methods based on costs and life cycle impact assessment indicators. *Int. J. Hydrogen Energ*. **2021,** *46*, 38612-38635.

[3] Ullah, N.; Ullah, S.; Khan, S.; Guziejewski, D.; Mirceski, V. A review: Metal-organic framework based electrocatalysts for methanol electro-oxidation reaction. *Int. J. Hydrogen Energ*. **2023,** *48*, 3340-3354.

[4] Mao, Q. Q.; Wang, P.; Wang, Z. Q.; Xu, Y.; Li, X. N.; Wang, L.; Wang, H. J. PdRh bimetallene for energy-saving hydrogen production via methanol electroreforming. *Appl. Mater. Today*. **2022,** *26*, 101400.

[5] Ullah, N.; Guziejewski, D. Formation of tungsten-doped molybdenum selenide electrocatalyst for methanol oxidation reaction. *Ionics*. **2023,** *29*, 2523-2527.

[6] Vij, V.; Sultan, S.; Harzandi, A. M.; Meena, A.; Tiwari, J. N.; Lee, W. G.; Yoon, T.; Kim, K. S. Nickel-Based electrocatalysts for energy-related applications: oxygen reduction, oxygen evolution, and hydrogen evolution reactions. *ACS Catal*. **2017,** *7*, 7196-7225.

[7] Sarwar, E.; Noor, T.; Iqbal, N.; Mehmood, Y.; Ahmed, S.; Mehek, R. Effect of Co-Ni ratio in graphene based bimetallic electro-catalyst for methanol oxidation. *Fuel. Cells*. **2018,** *18*, 189-194.

[8] Hutton, L. A.; Vidotti, M.; Patel, A. N.; Newton, M. E.; Unwin, P. R.; Macpherson, J. V. Electrodeposition of nickel hydroxide nanoparticles on boron-doped diamond electrodes for oxidative electrocatalysis. *J. Phys. Chem. C*. **2011,** *115*, 1649-1658.

[9] Sun, H. M.; Liu, J.; Zhang, C.; Yuan, Q. L.; Ye, Y. X.; Yan, W. S.; Tian, Z. F.; Liang, C. H. S, N dual-doped carbon nanotubes as substrate to enhance the methanol oxidation performance of NiO nanoparticles. *Carbon*. **2019,** *152*, 114-119.

[10] Wu, N.; Zhai, M. X.; Chen, F.; Zhang, X.; Guo, R. H.; Hu, T. P.; Ma, M. M. Nickel nanocrystal/nitrogen-doped carbon composites as efficient and carbon monoxide-resistant electrocatalysts for methanol oxidation reactions. *Nanoscale*. **2020,** *12*, 21687-21694.

[11] Zhu, H.; Wang, J. T.; Liu, X. L.; Zhu, X. M. Three-dimensional porous graphene supported Ni nanoparticles with enhanced catalytic performance for Methanol electrooxidation. *Int. J. Hydrogen Energ*. **2017,** *42*, 11206-11214.

[12] Guo, R. H.; Zhang, Y. J.; Zhang, X. T.; Hu, T. P. Ni/NiO heterojunction anchored on N-doped carbon for the enhanced methanol oxidation. *J. Alloys Compd*. **2023,** *960*, 170886.

[13] Ding, J. J.; Ma, L.; Gan, M. Y.; Zhan, W.; Zhou, C. L.; Wei, D. Y.; Han, S. C.; Shen, J.; Xie, F.; Zhong, X. J. Facile fabrication of ultrafine Pt nanoparticles supported on 3D macro-/oversized mesoporous N-doped carbon for efficient methanol oxidation. *Int. J. Hydrogen Energ*. **2019,** *44*, 30388-30400.

[14] Halim, E. M.; Perrot, H.; Sel, O.; Debiemme Chouvy, C.; Lafdi, K.; El Rhazi, M. Electrosynthesis of hierarchical Cu_2O-$Cu(OH)_2$ nanodendrites supported on carbon nanofibers/poly(para-phenylenediamine) nanocomposite as high-efficiency catalysts for methanol electrooxidation. *Int. J. Hydrogen Energ*. **2021,** *46*, 19926-19938.

[15] Yang, Y.; Guo, Y. F.; Fu, C.; Zhang, R. H.; Zhan, W.; Wang, P.; Zhang, X.; Wang, Q.; Zhou, X. W. In-situ loading synthesis of graphene supported PtCu nanocube and its high activity and stability for methanol oxidation reaction. *J. Colloid Interf. Sci*. **2021,** *595*, 107-117.

[16] Li, M. M.; Jiang, Q. G.; Yan, M. M.; Wei, Y. J.; Zong, J. B.; Zhang, J. F.; Wu, Y. P.; Huang, H. J. Three-dimensional boron- and nitrogen-codoped graphene aerogel-supported Pt nanoparticles as highly active electrocatalysts for methanol oxidation reaction. *ACS Sustainable Chem. Eng*. **2018,** *6*, 6644-6653.

[17] Zhang, J. J.; Sui, X. L.; Huang, G. S.; Gu, D. M.; Wang, Z. B. Hierarchical carbon coated molybdenum dioxide nanotubes as a highly active and durable electrocatalytic support for methanol oxidation. *J. Mater. Chem. A*. **2017,** *5*, 4067-4074.
[18] Rezaee, S.; Shahrokhian, S. Facile synthesis of petal-like NiCo/NiO-CoO/nanoporous carbon composite based on mixed-metallic MOFs and their application for electrocatalytic oxidation of methanol. *Appl. Catal. B: Environ*. **2019,** *244*, 802-813.
[19] Wang, N.; Hei, Y. S.; Liu, J. J.; Sun, M. M.; Sha, T. Z.; Hassan, M.; Bo, X. J.; Guo, Y. N.; Zhou, M. Low-cost and environment-friendly synthesis of carbon nanorods assembled hierarchical meso-macroporous carbons networks aerogels from natural apples for the electrochemical determination of ascorbic acid and hydrogen peroxide. *Anal. Chim. Acta.* **2019,** *1047*, 36-44.
[20] Sha, T. Z.; Liu, J. J.; Sun, M. M.; Li, L.; Bai, J.; Hu, Z. Q.; Zhou, M. Green and low-cost synthesis of nitrogen-doped graphene-like mesoporous nanosheets from the biomass waste of okara for the amperometric detection of vitamin C in real samples. *Talanta*. **2019,** *200*, 300-306.
[21] Lei, Y. X.; Sun, W.; Tiwari, S. K.; Thummavichai, K.; Ola, O.; Qin, X. P.; Ma, Z. Y.; Wang, N. N.; Zhu, Y. Q. Zn/Co-ZIF reinforced sugarcane bagasse aerogel for highly efficient catalytic activation of peroxymonosulfate. *J. Environ. Chem. Eng*. **2021,** *9*, 106885.
[22] Liu, T. T.; Li, M.; Bo, X. J.; Zhou, M. Designing transition metal alloy nanoparticles embedded hierarchically porous carbon nanosheets as high-efficiency electrocatalysts toward full water splitting. *J. Colloid Interf. Sci.* **2019,** *537*, 280-294.
[23] Li, M.; Liu, X. T.; Xiong, Y. P.; Bo, X. J.; Zhang, Y. F.; Han, C.; Guo, L. P. Facile synthesis of various highly dispersive CoP nanocrystal embedded carbon matrices as efficient electrocatalysts for the hydrogen evolution reaction. *J. Mater. Chem. A*. **2015,** *3*, 4255-4265.
[24] Li, M.; Han, C.; Zhang, Y. F.; Bo, X. J.; Guo, L. P. Facile synthesis of ultrafine Co_3O_4 nanocrystals embedded carbon matrices with specific skeletal structures as efficient non-enzymatic glucose sensors. *Anal. Chim. Acta.* **2015,** *861*, 25-35.
[25] Zhu, J. Y.; Chen, S. Q.; Xue, Q.; Li, F. M.; Yao, H. C.; Xu, L.; Chen, Y. Hierarchical porous Rh nanosheets for methanol oxidation reaction. *Appl. Catal. B: Environ*. **2020,** *264*, 118520.
[26] Yao, Q.; Huang, B. L.; Zhang, N.; Sun, M. Z.; Shao, Q.; Huang, X. Q. Channel-rich RuCu nanosheets for pH-universal overall water splitting electrocatalysis. *Angew. Chem. Int. Edit*. **2019,** *58*, 13983-13988.
[27] Zhang, L. M.; Sui, X. L.; Zhao, L.; Zhang, J. J.; Gu, D. M.; Wang, Z. B. Nitrogen-doped carbon nanotubes for high-performance platinum-based catalysts in methanol oxidation reaction. *Carbon*. **2016,** *108*, 561-567.
[28] Naveen Kumar, T. R.; Swamynadhan, M.; Ghosh, S.; Neppolian, B. Boron-induced oxygen vacancies for methanol oxidation reaction: selectivity towards formate via non-noble metals. *Sustain. Energ. Fuels*. **2022,** *6*, 3573-3581.
[29] Yin, P. Q.; Yao, T.; Wu, Y. E.; Zheng, L. R.; Lin, Y.; Liu, W.; Ju, H. X.; Zhu, J. F.; Hong, X.; Deng, Z. X.; Zhou, G.; Wei, S. Q.; Li, Y. D. Single cobalt atoms with precise N-coordination as superior oxygen reduction reaction catalysts. *Angew. Chem. Int. Edit.* **2016,** *55*, 10800-10805.
[30] Sun, H. M.; Ye, Y. X.; Liu, J.; Tian, Z. F.; Cai, Y. Y.; Li, P. F.; Liang, C. H. Pure Ni nanocrystallines anchored on rGO present ultrahigh electrocatalytic activity and stability in methanol oxidation. *Chem. Commun*. **2018,** *54*, 1563-1566.
[31] Xu, Y. G.; Ullah, N.; Chen, L. L.; Wei, W.; Oluigbo, C. J.; Xie, M.; Zhang, M. M.; Xie, J. M. Nickel loaded graphene-like carbon sheets an improved electrocatalyst for hydrogen evolution reaction. *Mater. Chem. Phys*. **2019,** *227*, 105-110.
[32] Pieta, I. S.; Rathi, A.; Pieta, P.; Nowakowski, R.; Hołdynski, M.; Pisarek, M.; Kaminska, A.; Gawande, M. B.; Zboril, R. Electrocatalytic methanol oxidation over Cu, Ni and bimetallic Cu-Ni nanoparticles supported on graphitic carbon nitride. *Appl. Catal. B: Environ*. **2019,** *244*, 272-283.
[33] Zhang, B. W.; Sheng, T.; Wang, Y. X.; Chou, S.; Davey, K.; Dou, S. X.; Qiao, S. Z. Long-life room-temperature sodium-sulfur batteries by virtue of transition-metal-nanocluster-sulfur interactions. *Angew. Chem. Int. Edit.* **2019,** *58*, 1484-1488.
[34] Ullah, N.; Xie, M.; Oluigbo, C. J.; Xu, Y. G.; Xie, J. M.; Rasheed, H. U.; Zhang, M. M. Nickel and cobalt in situ grown in 3-dimensional hierarchical porous graphene for effective methanol electro-oxidation reaction. *Electroanal. Chem*. **2019,** *838*, 7-15.
[35] Wang, J.; Teschner, D.; Yao, Y. Y.; Huang, X.; Willinger, M.; Shao, L. D.; Schlögl, R. Fabrication of nanoscale NiO/Ni heterostructures as electrocatalysts for efficient methanol oxidation. *J. Mater. Chem. A*. **2017,** *5*, 9946-9951.

[36] Dinh, K. N.; Zheng, P. L.; Dai, Z. F.; Zhang, Y.; Dangol, R.; Zheng, Y.; Li, B.; Zong, Y.; Yan, Q. Y. Ultrathin porous NiFeV ternary layer hydroxide nanosheets as a highly efficient bifunctional electrocatalyst for overall water splitting. *Small*. **2018,** *14*, 1703257.
[37] Sun, X. H.; Shao, Q.; Pi, Y. C.; Guo, J.; Huang, X. Q. A general approach to synthesise ultrathin NiM (M = Fe, Co, Mn) hydroxide nanosheets as high-performance low-cost electrocatalysts for overall water splitting. *J. Mater. Chem. A*. **2017,** *5*, 7769-7775.
[38] Bo, X.; Li, Y. B.; Hocking, R. K.; Zhao, C. NiFeCr hydroxide holey nanosheet as advanced electrocatalyst for water oxidation. *ACS Appl. Mater. Interfaces*. **2017,** *9*, 41239-41245.
[39] Hussain, S.; Ullah, N.; Zhang, Y. Y.; Shaheen, A.; Javed, M. S.; Lin, L. Y.; Zulfiqar; Shah, S. B.; Liu, G. W.; Qiao, G. J. One-step synthesis of unique catalyst Ni9S8@C for excellent MOR performances. *Int. J. Hydrogen Energ*. **2019,** *44*, 24525-24533.
[40] Wang, L. X.; Li, Y.; Xia, M. R.; Li, Z. P.; Chen, Z. H.; Ma, Z. P.; Qin, X. J.; Shao, G. J. Ni nanoparticles supported on graphene layers: An excellent 3D electrode for hydrogen evolution reaction in alkaline solution. *J. Power Sources*. **2017,** *347*, 220-228.
[41] Mansor, M.; Timmiati, S. N.; Lim, K. L.; Wong, W. Y.; Kamarudin, S. K.; Nazirah Kamarudin, N. H. Recent progress of anode catalysts and their support materials for methanol electrooxidation reaction. *Int. J. Hydrogen Energ*. **2019,** *44*, 14744-14769.
[42] Wang, L. Y.; Zhang, G. G.; Liu, Y.; Li, W. F.; Lu, W.; Huang, H. T. Facile synthesis of a mechanically robust and highly porous NiO film with excellent electrocatalytic activity towards methanol oxidation. *Nanoscale*. **2016,** *8*, 11256-11263.
[43] Fu, G. T.; Yan, X. X.; Cui, Z. M.; Sun, D. M.; Xu, L.; Tang, Y. W.; Goodenough, J. B.; Lee, J. M. Catalytic activities for methanol oxidation on ultrathin $CuPt_3$ wavy nanowires with/without smart polymer. *Chem. Sci*. **2016,** *7*, 5414-5420.
[44] Wang, Q.; Zhao, Z. L.; Jia, Y. L.; Wang, M. P.; Qi, W. H.; Pang, Y.; Yi, J.; Zhang, Y. F.; Li, Z.; Zhang, Z. Unique Cu@CuPt core-shell concave octahedron with enhanced methanol oxidation activity. *ACS Appl. Mater. Interfaces*. **2017,** *9*, 36817-36827.
[45] Shi, X. Q.; Wen, Y.; Guo, X. Y.; Pan, Y. X.; Ji, Y. Y.; Ying, Y.; Yang, H. F. Dentritic CuPtPd catalyst for enhanced electrochemical oxidation of methanol. *ACS Appl. Mater. Interfaces*. **2017,** *9*, 25995-26000.
[46] Chen, L. S.; Hua, Z. L.; Shi, J. L.; He, M. Y. CuO/$Co(OH)_2$ nanosheets: a novel kind of electrocatalyst for highly efficient electrochemical oxidation of methanol. *ACS Appl. Mater. Interfaces*. **2018,** *10*, 39002-39008.
[47] Du, J. N.; You, S. J.; Li, X. R.; Tang, B.; Jiang, B. J.; Yu, Y.; Cai, Z.; Ren, N. Q.; Zou, J. L. In situ crystallization of active NiOOH/CoOOH heterostructures with hydroxide Ion adsorption sites on velutipes-like CoSe/NiSe nanorods as catalysts for oxygen evolution and cocatalysts for methanol oxidation. *ACS Appl. Mater. Interfaces*. **2020,** *12*, 686-697.
[48] Yang, B.; Yu, Y.; Qiao, J.; Yuan, L.; Shen, X.; Hu, X. Solution plasma method for the preparation of Cu-Ni/CuO-NiO with excellent methanol electrocatalytic oxidation performance. *Appl. surf. Sci*. **2020,** *513*, 145808.
[49] Zhang, Y.; Zhao, J.; Kang, X.; Chen, G.; Li, Y. Synthesis the flower-like N-C/NiO nanocomposites by one-pot hydrothermal method as efficient electrocatalyst for methanol oxidation in alkaline electrolyte. *Colloid. Surface A*. **2021,** *629*, 127466.
[50] Sun, H.; Liu, J.; Zhang, C.; Yuan, Q.; Ye, Y.; Yan, W.; Tian, Z.; Liang, C. S, N dual-doped carbon nanotubes as substrate to enhance the methanol oxidation performance of NiO nanoparticles. *Carbon*. **2019,** *152*, 114-119.
[51] Dubale, A. A.; Zheng, Y.; Wang, H.; Hubner, R.; Li, Y.; Yang, J.; Zhang, J.; Sethi, N. K.; He, L.; Zheng, Z.; Liu, W. High-performance bismuth-doped nickel aerogel electrocatalyst for the methanol oxidation reaction. *Angew. Chem. Int. Ed. Engl*. **2020,** *59*, 13891-13899.
[52] Candelaria, S. L.; Bedford, N. M.; Woehl, T. J.; Rentz, N. S.; Showalter, A. R.; Pylypenko, S.; Bunker, B. A.; Lee, S.; Reinhart, B.; Ren, Y.; Ertem, S. P.; Coughlin, E. B.; Sather, N. A.; Horan, J. L.; Herring, A. M.; Greenlee, L. F. Multi-component Fe-Ni hydroxide nanocatalyst for oxygen evolution and methanol oxidation reactions under alkaline conditions. *ACS Catalysis*. **2016,** *7*, 365-379.
[53] Sun, H.; Ye, Y.; Liu, J.; Tian, Z.; Cai, Y.; Li, P.; Liang, C. Pure Ni nanocrystallines anchored on rGO present ultrahigh electrocatalytic activity and stability in methanol oxidation. *Chem. Commun. (Camb)*. **2018,** *54*, 1563-1566.
[54] Wu, D.; Zhang, W.; Cheng, D. Facile synthesis of Cu/NiCu electrocatalysts integrating alloy, core-shell, and one-dimensional structures for efficient methanol oxidation reaction. *ACS Appl. Mater. Interfaces*. **2017,** *9*, 19843-19851.

[55] Chen, L.; Hua, Z.; Shi, J.; He, M. CuO/$Co(OH)_2$ Nanosheets: A novel kind of electrocatalyst for highly efficient electrochemical oxidation of methanol. *ACS Appl. Mater. Interfaces*. **2018,** *10*, 39002-39008.
[56] Song, X.; Sun, Q.; Gao, L.; Chen, W.; Wu, Y.; Li, Y.; Mao, L.; Yang, J.-H. Nickel phosphate as advanced promising electrochemical catalyst for the electro-oxidation of methanol. *Int. J. Hydrogen Energ*. **2018,** *43*, 12091-12102.
[57] Tong, X.; Qin, Y.; Guo, X.; Moutanabbir, O.; Ao, X.; Pippel, E.; Zhang, L.; Knez, M. Enhanced catalytic activity for methanol electro-oxidation of uniformly dispersed nickel oxide nanoparticles-carbon nanotube hybrid materials. *Small*. **2012,** *8*, 3390-3395.

Appendix

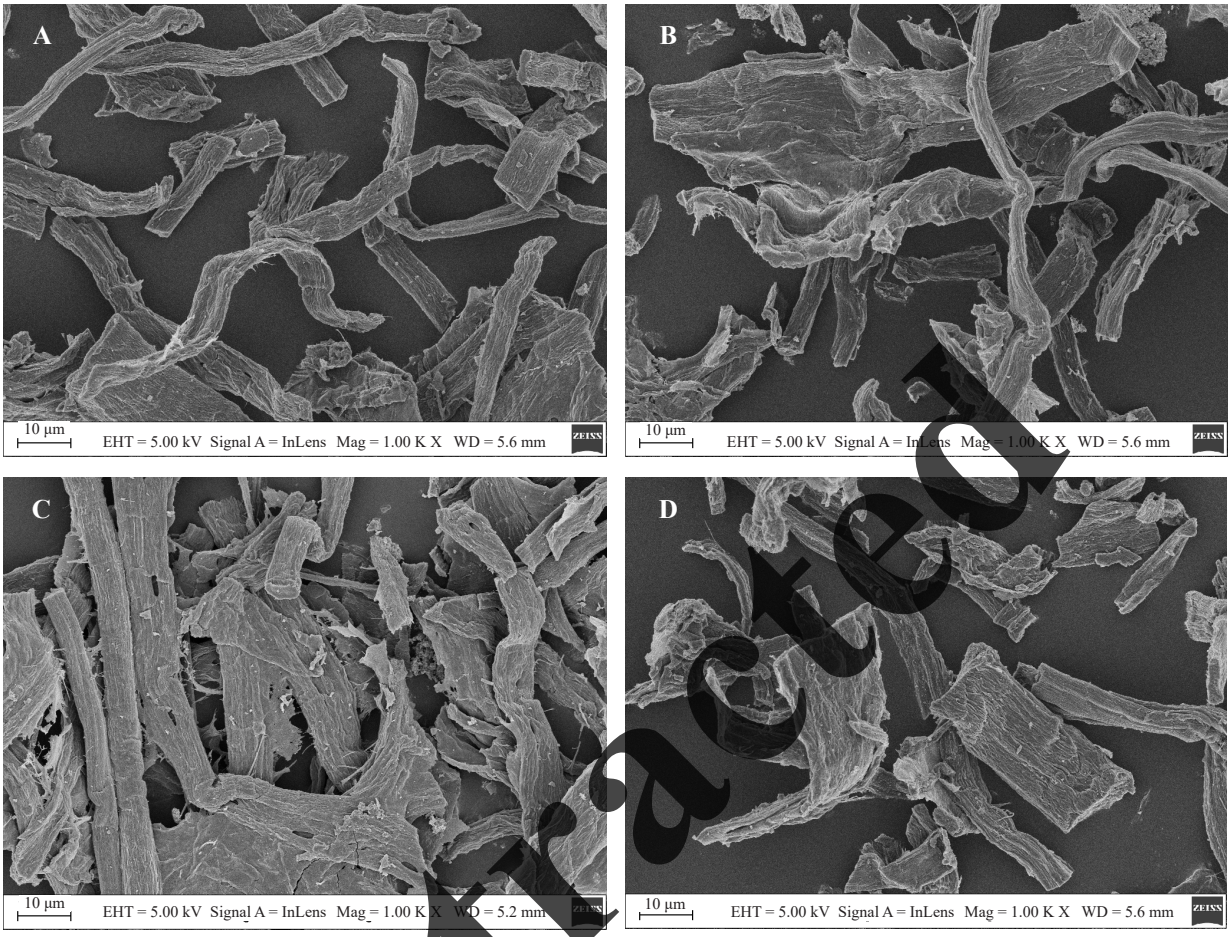

Figure S1. SEM images of the NiNPs/T-dNPCNs$_{600}$ (A), the NiNPs/T-dNPCNs$_{700}$ (B), the NiNPs/T-dNPCNs$_{800}$ (C) and the NiNPs/T-dNPCNs$_{900}$ (D)

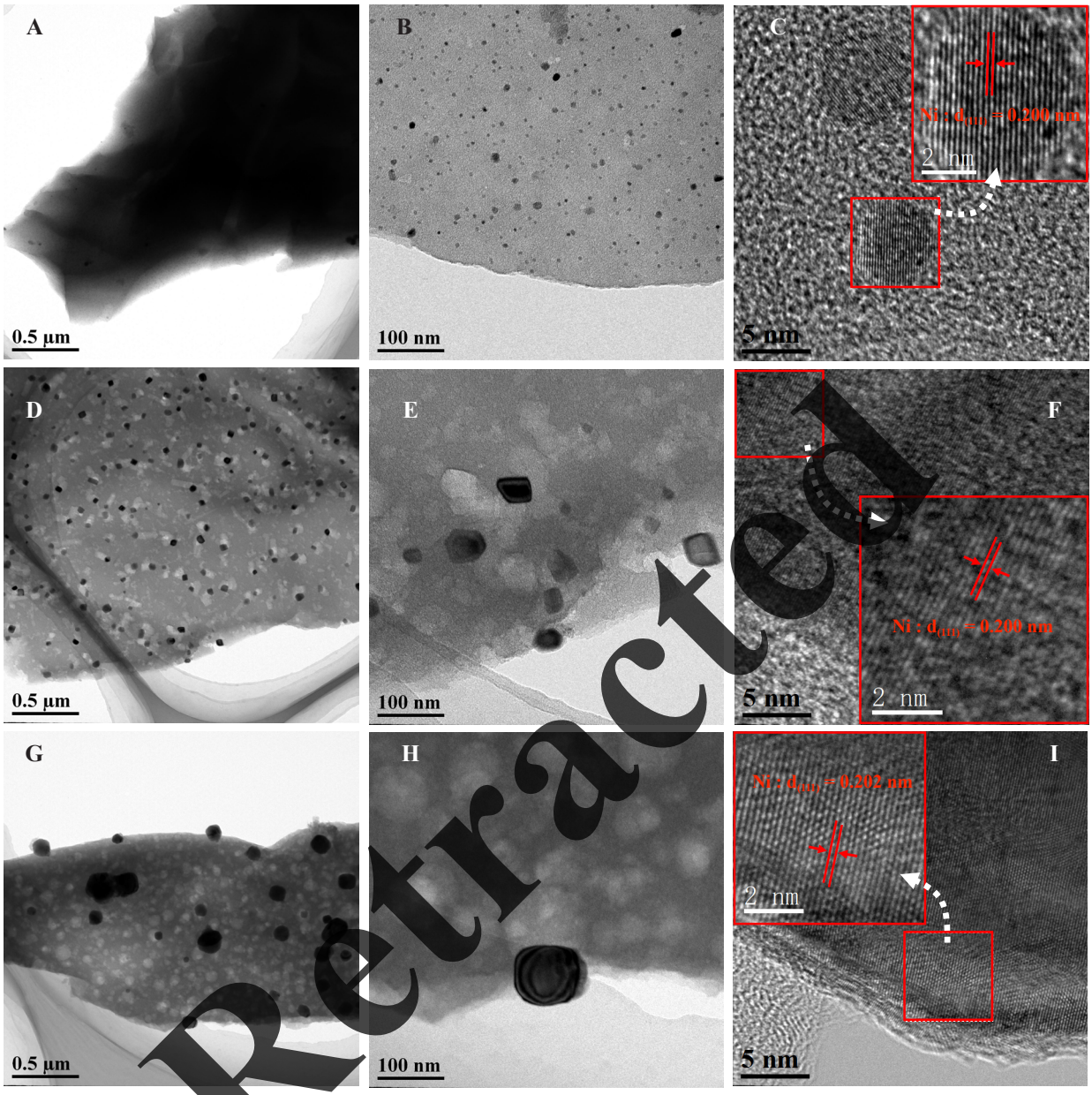

Figure S2. TEM images of the NiNPs/T-dNPCNs$_{600}$ (A-C), the NiNPs/T-dNPCNs$_{700}$ (D-F) and the NiNPs/T-dNPCNs$_{900}$ (G-I). HRTEM images of the NiNPs/T-dNPCNs$_{600}$ (C), the NiNPs/T-dNPCNs$_{700}$ (F) and the NiNPs/T-dNPCNs$_{900}$ (I)

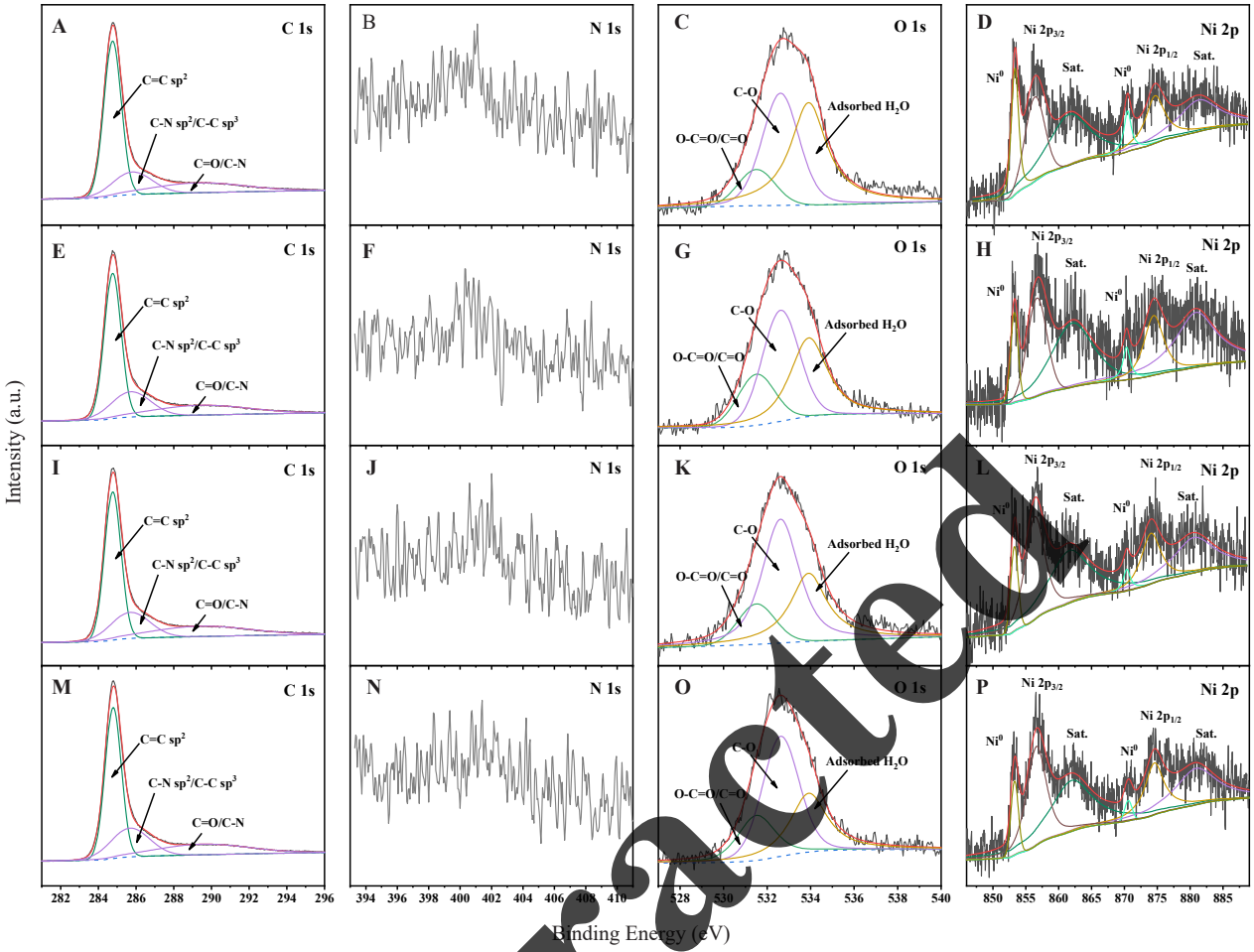

Figure S3. XPS spectra of C 1s (A), N 1s (B), O 1s (C) and Ni 2p (D) of the NiNPs/T-dNPCNs$_{600}$; XPS spectra of C 1s (E), N 1s (F), O 1s (G) and Ni 2p (H) of the NiNPs/T-dNPCNs$_{700}$; XPS spectra of C 1s (I), N 1s (J), O 1s (K) and Ni 2p (L) of the NiNPs/T-dNPCNs$_{800}$; XPS spectra of C 1s (M), N 1s N), O 1s (O) and Ni 2p (P) of the NiNPs/T-dNPCNs$_{900}$

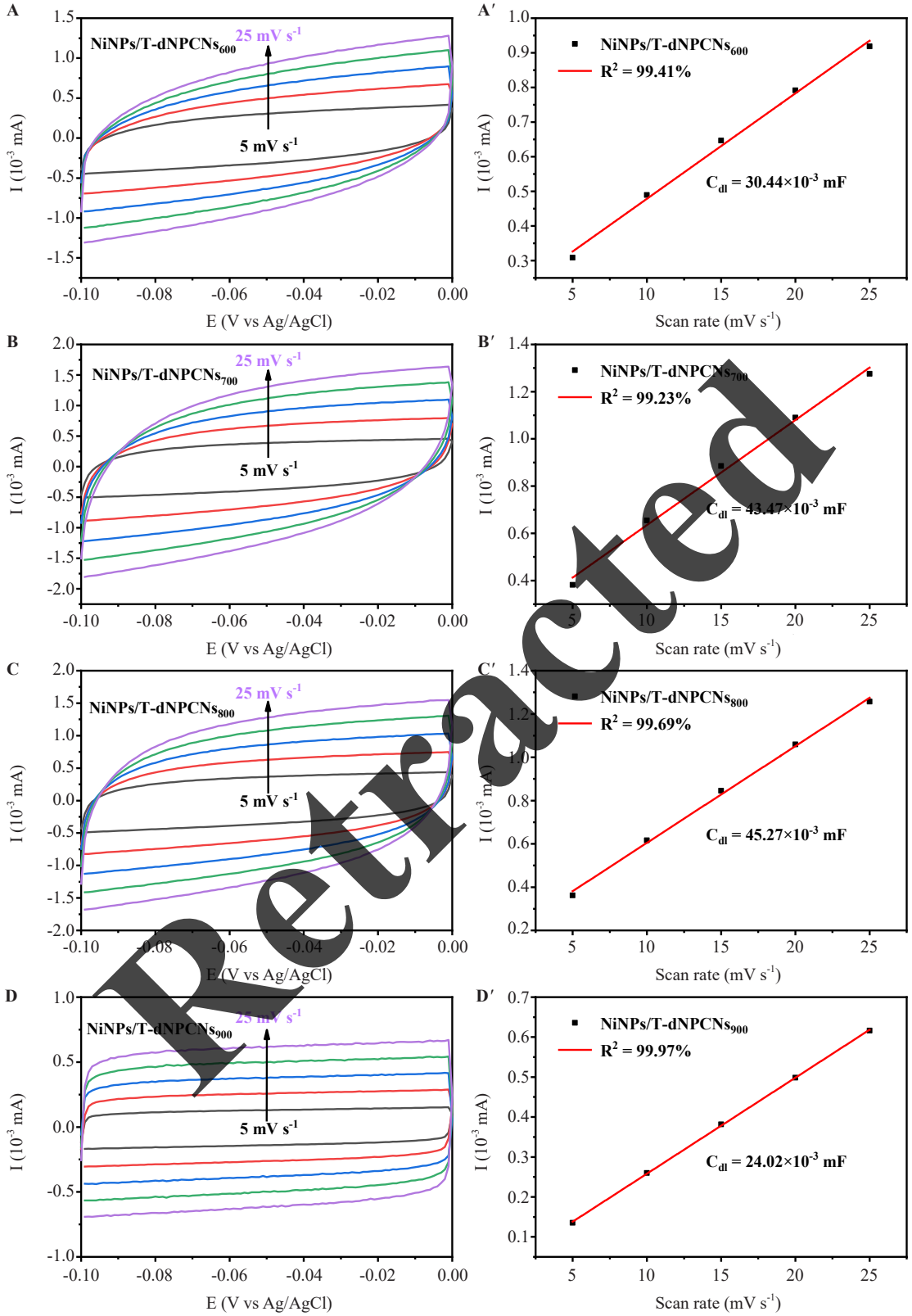

Figure S4. CV curves of (A) the NiNPs/T-dNPCNs$_{600}$/GCE, (B) the NiNPs/T-dNPCNs$_{700}$/GCE, (C) the NiNPs/T-dNPCNs$_{800}$/GCE and (D) the NiNPs/T-dNPCNs$_{900}$/GCE from -0.1 V to -0 V vs Ag/AgCl at scan rates of 5, 10, 15, 20 and 25 mV · s^{-1} in 1.0 M KOH. The capacitive current ((I_a - I_c)/2) at -0.05 V vs Ag/AgCl as a function of various scan rates for (A′) the NiNPs/T-dNPCNs$_{600}$/GCE, (B′) the NiNPs/T-dNPCNs$_{700}$/GCE, (C′) the NiNPs/T-dNPCNs$_{800}$/GCE and (D′) the NiNPs/T-dNPCNs$_{900}$/GCE; the C_{dl} equal to the slopes

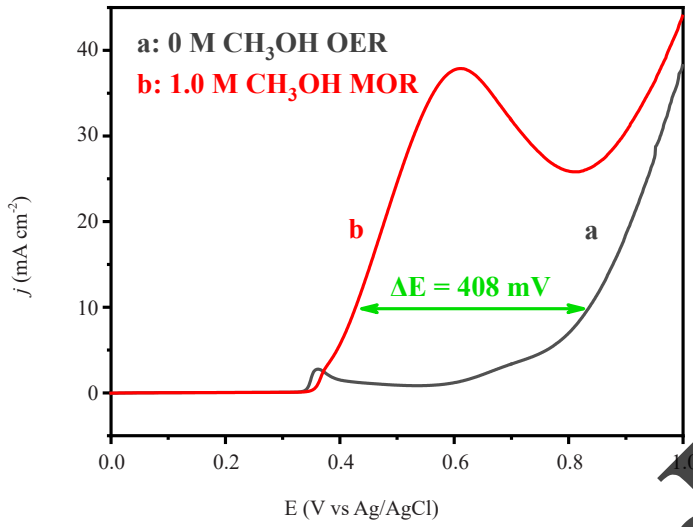

Figure S5. Linear sweep voltammetry curves of the NiNPs/T-dNPCNs$_{800}$/GCE. Specific activity normalized by the geometric area of the modified electrode

Table S1. Comparison of mass activity between non-precious metal catalysts in this study and reported catalysts for MOR

Catalyst	Specific activity mA · cm^{-2}	Mass activity mA · mg^{-1}	CH_3OH concentration mol · L^{-1}	Scanning rate mV · s^{-1}	Ref.
Cu-Ni/CuO-NiO/GNs	152	3,563	0.5	50	48
flower-like N-C/NiO	26.6	3,298	1	50	49
NiO/S, N-doped Carbon nanotube	-	2,200	1	50	50
$Ni_{97}Bi_3$ aerogel	199	1,830	1	50	51
Fe-Ni hydroxide nanocatalyst	49	1,709	1	20	52
Ni/rGO	-	1,600	1	50	53
Cu/NiCuNWs-220/C	34.9	867.1	1	50	54
CuO/$Co(OH)_2$	159	764	3	50	55
Meso NiPO NS	44.97[#]	636	0.5	50	56
NiO/CNT	128	498	1	50	57
Pt/C	-	485	1	50	This work
NiNPs/T-dNPCNs$_{600}$	0.413	1,312	1	50	This work
NiNPs/T-dNPCNs$_{700}$	0.754	2,991	1	50	This work
NiNPs/T-dNPCNs$_{900}$	0.627	1,432	1	50	This work
NiNPs/T-dNPCNs$_{800}$	0.885	3,349	1	50	This work

[#] (normalized by the geometric area of the electrode)